

1 **Processes influencing formation of low-salinity high-biomass lenses near**
2 **the edge of the Ross Ice Shelf**

3
4 Yizhen Li¹, Dennis J. McGillicuddy Jr.¹, Michael S. Dinniman², and John M. Klinck²

5 ¹Department of Applied Ocean Physics and Engineering, Woods Hole Oceanographic Institution,
6 Woods Hole, MA 02543

7 ²Center for Coastal Physical Oceanography, Old Dominion University, Norfolk, Virginia 23529,
8 USA

9 Correspondence: Yizhen Li, Phone: 508-289-2238, Email: yzli@whoi.edu

10
11 **Abstract**

12 Both remotely sensed and *in situ* observations in austral summer of early 2012 in the Ross Sea
13 suggest the presence of cold, low-salinity, and high-biomass eddies along the edge of the Ross Ice
14 Shelf (RIS). Satellite measurements include sea surface temperature and ocean color, and
15 shipboard data sets include hydrographic profiles, towed instrumentation, and underway acoustic
16 Doppler current profilers. Idealized model simulations are utilized to examine the processes
17 responsible for ice shelf eddy formation. 3-D model simulations produce similar cold and fresh
18 eddies, although the simulated vertical lenses are quantitatively thinner than observed. Model
19 sensitivity tests show that both basal melting underneath the ice shelf and irregularity of the ice
20 shelf edge facilitate generation of cold and fresh eddies. 2-D model simulations further suggest
21 that both basal melting and downwelling-favorable winds play crucial roles in forming a thick
22 layer of low-salinity water observed along the edge of the RIS. These properties may have been
23 entrained into the observed eddies, whereas that entrainment process was not captured in the
24 specific eddy formation events studied in our 3-D model—which may explain the discrepancy
25 between the simulated and observed eddies, at least in part. Additional sensitivity experiments
26 imply that uncertainties associated with background stratification and wind stress may also
27 explain why the model underestimates the thickness of the low-salinity lens in the eddy interiors.
28 Our study highlights the importance of incorporating accurate wind forcing, basal melting, and
29 ice shelf irregularity for simulating eddy formation near the RIS edge. The processes responsible

30 for generating the high phytoplankton biomass inside these eddies remain to be elucidated.

31 **Key words:** eddies, instability, basal melting, mixed layer processes, ice shelf geometry

32

33 **1. Introduction**

34 The Ross Ice Shelf (RIS) is the largest ice shelf ($\sim 4.7 \times 10^5 \text{ km}^2$) in Antarctica,
35 located in the southern Ross Sea (Fig. 1). The RIS region plays host to a number of
36 important physical and biological processes. Air-sea interaction and ice dynamics at the
37 edge of the RIS influence High Salinity Shelf Water (HSSW) formation (MacAyeal, 1984;
38 Orsi and Wiederwohl, 2009), which is a dense water mass that is critical in Antarctic
39 Bottom Water formation (Jacobs et al., 1996; Orsi et al., 2002; Whitworth and Orsi, 2006;
40 Gordon et al., 2009). The frontal region also bridges heat and mass exchanges with the
41 open ocean (Rignot et al., 2013; Depoorter et al., 2013). The Ross Sea is one of the most
42 biologically productive areas in the Southern Ocean (Comiso et al., 1993; Arrigo et al.,
43 1998; Smith et al., 2014), and the RIS delimits the southern boundary of the region of
44 high productivity. Iron supply is thought to regulate primary production in the Ross Sea
45 (Arrigo, 2003; Martin et al., 1990; Sedwick et al., 2000). Although recent evidence
46 suggests that the iron supply from glacial ice melt constitutes only a small fraction of the
47 iron supply to this region (McGillicuddy et al., 2015), basal melting is a primary pathway
48 for iron supply in other Antarctic polynyas (Arrigo et al., 2015; Gerringa et al., 2012).

49 Processes at different depth levels make the cavity underneath the RIS a complex
50 ocean environment. Near the ice shelf front, increased melting is facilitated by occasional
51 warm water intrusions (Jenkins and Doake, 1991) from adjacent upper ocean waters that
52 come in contact with the edge of the ice shelf. At mid depth, melting is caused by intrusion
53 of modified circumpolar deep water (Jacobs et al., 2011, Dinniman et al., 2007, 2012;
54 Klinck and Dinniman, 2010; Pritchard et al., 2012). In the deepest layer, dense HSSW (a
55 product of brine rejection over the continental shelf from ice formation during the winter
56 months), which is at the surface freezing point, can penetrate into the cavity, causing
57 melting near the grounding line due to the depression of the freezing point of seawater
58 with increasing pressure. As the buoyant meltwaters rise along the ice shelf base, they can
59 re-freeze at mid-depth due to the increase in freezing point with decreasing pressure,
60 producing super-cooled Ice Shelf Water (ISW). All these processes interact with each

61 other at various spatial and temporal scales, making for a complex regime of
62 thermohaline circulation (MacAyeal, 1984; 1985).

63 Of particular interest from the ecosystem perspective is the penetration of glacial
64 meltwater into the surface waters in the interior of the Ross Sea, as this constitutes a
65 source of iron to upper ocean phytoplankton populations. Although the iron supply from
66 glacial meltwater is thought to be small relative to other sources in the Ross Sea
67 (McGillicuddy et al., 2015), physical processes such as oceanic eddies that affect the
68 glacial meltwater may be locally important to the initiation and spatial distribution of
69 regional phytoplankton blooms. In austral summer of 2012, we observed two anticyclonic
70 eddies emanating from the edge of the RIS northward into the Ross Sea. The eddies
71 contained low-salinity lenses with deep mixed layers (ca. 80 m) and very high biomass of
72 the colonial prymnesiophyte *Phaeocystis antarctica* (Smith et al., submitted). Our goal is
73 to identify the processes that lead to generation of these eddy features, which will set the
74 stage for future study of the physical-biological interactions leading to the high biomass
75 observed in their interiors.

76 The primary surface circulation feature along the front of the RIS in this area is a
77 relatively strong, narrow, and fresh coastal current that flows to the west (Jacobs et al.,
78 1970; Keys et al., 1990). A similar westward current is found along the front of the
79 Ronne-Filchner Ice Shelf (Makinson et al., 2006) where mooring observations at depth
80 (as deep as 200-400 m) also suggest the possibility of eddy-driven variability (Nicholls et
81 al., 2003). Knowledge of ocean variability in the near-surface ocean layer near the RIS
82 remains rather limited due the scarcity of data, with relatively few direct observations
83 available (Jacobs et al., 1985; Smethie and Jacobs, 2005). Arzeno et al. (2014) postulated
84 eddies as being responsible for variability in currents underneath the RIS that was
85 uncorrelated with the wind. Although the process of eddy generation has been examined
86 in many oceanic regimes, relatively few studies have focused on instabilities associated
87 with ice-ocean interactions (Clarke et al., 1978; Chu, 1987; Dumont et al., 2010;

88 Häkkinen, 1986; Niebauer, 1982). In general, glacial meltwater can create horizontal
89 density gradients that force a baroclinic jet (Niebauer, 1982). Häkkinen (1986) found that
90 when across- and along-ice edge spatial scales are similar enough, such baroclinic jets
91 can generate eddy structures along the ice edge, especially when the wind forcing is
92 time-varying between upwelling and downwelling conditions. In a modeling study in
93 Baffin Bay near Greenland, cyclonic eddies were generated at the edge of landfast ice in
94 response to frequent northerly wind forcing (Dumont et al., 2010). All of these studies
95 pointed to the importance of baroclinic jets and wind forcing in forming eddies near the
96 ice edge.

97 Earlier efforts utilized idealized two-layer ocean models to study how ice-ocean
98 interactions can excite unstable wave forms. Using a semi-analytical quasi-geostrophic
99 model, Clark et al. (1978) showed that fluctuations in the flow along fast ice can be
100 described as wind-forced trapped long-waves propagating along the ice edge. Chu (1987)
101 used a similar framework, identifying an air-sea interaction feedback mechanism that
102 excites an unstable mode in the presence of curvature in the ice edge. Both Clark (1978)
103 and Chu (1987) highlighted the importance of considering multiple factors such as ice
104 shelf edge irregularity and background stratification (initial conditions) in studying the
105 instability processes. However, because their models did not consider basal melting, they
106 were not able to capture the structure of low salinity features near the ice edge.

107 Our approach is to use high-resolution models with varying levels of complexity to
108 understand the mesoscale phenomena we observed at the edge of the RIS. In section 2 we
109 present the observations, consisting of both satellite imagery and *in situ* measurements.
110 We describe the model configuration in section 3, followed by sections 4 and 5 showing
111 its implementation in three- and two-dimensional configurations respectively. The former
112 is used to investigate the process responsible for eddy generation, whereas the latter
113 provides insight into the mechanisms responsible for the thickness of the low-salinity
114 surface layer. Section 6 offers further analysis and discussion of the dynamics via

115 sensitivity analyses. A summary and conclusions are presented in section 7.

116

117 **2. Observations**

118

119 2.1 Satellite imagery

120 A sequence of satellite images in January 2012 captured the signature and evolution
121 of several eddies near the RIS. On January 22, there were a number of cold eddies along
122 the edge of the ice shelf (Fig. 2a), including some that were already separated from the
123 RIS (e.g., near 177.5°E), and some that remained connected to the ice shelf edge (e.g.,
124 Eddy 1 and Eddy 2). Eddy 1 (radius ~ 12 km) was flanked by warm anomalies to the east
125 and northwest. Eddy 2 was slightly smaller (radius ~ 8 km), separated from Eddy 1 by a
126 warm filament protruding south to the edge of the RIS. Satellite ocean color imagery
127 indicated a ca. 20 km wide strip of low chlorophyll *a* (Chl-*a*) concentrations extending
128 along the edge of the RIS, with much higher concentrations to the north (Fig. 2b). The
129 signatures of Eddies 1 and 2 in ocean color are barely discernible in the January 22 image
130 as northward perturbations to the frontal boundary separating high and low Chl-*a*.

131 Three days later, the two eddies had moved away from the RIS and evolved in the
132 process (Fig. 3). Both eddies appear to be warmer, and have similar radii that are still
133 larger than the local Rossby deformation radius (~ 5 km). Eddy 1 moved north-northwest,
134 whereas Eddy 2 moved northwest, narrowing the gap in between them. Both eddies
135 propagated westward, as is commonly the case due to meridional variation in the Coriolis
136 parameter (Cushman-Roisin et al., 1990), although the background westward flow in this
137 region may play a crucial role. Compared to three days prior, Eddy 1 took on a more
138 circular shape. By January 25, Eddy 1 had almost completely separated from the RIS,
139 connected to the shelf edge by only narrow cold filaments running southwest from the
140 southern flank of the eddy and south from the eastern flank of the eddy (Fig. 3a). The
141 warm anomaly previously to the east of Eddy 1 on January 22 appeared to have been
142 swept southwestward by January 25. However, this movement is opposite in direction to

143 that caused by the eddy's counterclockwise rotation (see shipboard velocity observations
144 described in the following section), so if this interpretation is correct then translation of
145 the warm anomaly must have been caused by flow external to the eddy. On January 25,
146 Eddy 2 was still in the process of separation from the ice shelf, with a cold filament
147 linking its southern flank to the cold-water band adjacent to the RIS. As the two eddy
148 features moved away from the RIS into the Ross Sea interior, they became more clearly
149 evident in ocean color imagery as local minima in Chl-a (Fig. 3b).

150

151 2.2 High-resolution survey of the RIS eddies

152 Voyage NBP-1201 of RVIB *Nathaniel B. Palmer* took place from December 24, 2011
153 to Feb 5, 2012. A multi-scale survey of the Ross Sea was carried out, and herein we focus
154 on a subset of the observations collected in the vicinity of the RIS. High-resolution
155 cross-sections of Eddies 1 and 2 were obtained with the Video Plankton Recorder (VPR;
156 Davis et al., 1992), providing conductivity, temperature and depth (CTD) observations,
157 along with fluorescence measurements and plankton imagery. Underway Acoustic
158 Doppler Current Profiler (ADCP) current velocity observations were collected along the
159 ship track with an RD Instruments NB150. Temperature, salinity, and fluorescence
160 profiles were obtained with a SeaBird Electronics 911 CTD and standard Rosette system.

161 A VPR survey of Eddies 1 and 2 was conducted on January 26 (magenta line, Fig. 3).
162 The ship track started from the west and cut through Eddy 1. It then passed across the
163 frontal area between the two eddies, penetrated into the interior of Eddy 2, and
164 subsequently turned southeastward. Along-track ADCP data suggests that both eddies are
165 anticyclonic (counterclockwise rotation), although the eastern flank of Eddy 2 was not
166 surveyed and thus the closed circulation of that feature cannot be validated. Also note that
167 the eddies were moving fast enough that we do not expect exact matchup of the *in situ*
168 observations with the satellite image due to differences in timing- e.g., the northward
169 swirl on the eastern flank of Eddy 1 observed with the shipboard ADCP is outside the

170 eddy core depicted in the satellite data. The VPR data revealed that the cores of both
171 eddies contained low-salinity lenses extending from the surface to 80-120 m (Fig. 4b).
172 The surface layer temperature was 0.6 °C lower than outside of the eddies (Fig 4a). The
173 mixed layers within the eddies were deeper than outside, where the surface layer of
174 relatively warm and salty water was only about 45 m deep (Fig. 4a, b). The cold and fresh
175 lenses in the eddy interiors contained higher fluorescence than ambient waters sampled
176 west of Eddy 1 (Fig. 4c), consistent with high abundance of *P. antarctica* colonies
177 identified in the VPR imagery (Smith et al., submitted). Highest fluorescence along the
178 ship track occurred at the frontal boundary on the western flank of Eddy 2 (where the
179 flow is southward as suggested by along-track ADCP, Fig. 3), although the mechanism
180 responsible for that submesoscale enhancement of fluorescence remains unknown.

181 It is interesting to note that the lenses of high fluorescence revealed by the VPR data
182 (Fig. 4c, d) were manifested as local minima in Chl-a in the satellite imagery (Fig. 3).
183 Caution needs to be taken in comparing *in situ* fluorescence and satellite data for several
184 reasons. First, the algorithm for retrieving MODIS Chl-a is based on water leaving
185 irradiance (Clark, 1997), and the Chl-a concentration reflects a weighted average over the
186 upper 1-2 optical depths. Second, remotely sensed Chl-a can also be contaminated by
187 other dissolved and particulate materials (Carder et al., 2004). Third, *in situ* fluorescence
188 can be reduced by the ‘quenching effect’ (e.g., Falkowski et al., 1995) when
189 photosynthetic reaction centers are saturated with ambient light, such as typically occurs
190 in the upper euphotic zone when daylight is abundant, which was always the case during
191 the cruise season.

192 Despite these caveats, it is still of interest to make direct comparisons between the
193 VPR observations of fluorescence and the satellite retrievals of Chl-a. In order to
194 compare the VPR observations with satellite data, one needs to take into account the
195 vertical extent over which the satellite observations pertain. The optical depth can be
196 estimated based on an inverse relationship with the attenuation coefficient of downward

197 irradiance (K_d) for blue light (http://oceancolor.gsfc.nasa.gov/cms/atbd/kd_490). Based
198 on satellite data from January 2012, K_d was within the range of 0.2-0.4 m^{-1} near the RIS
199 edge (not shown), indicating an optical depth of ~ 5 m. Comparison of the VPR
200 fluorescence averaged over upper two optical depths (10 m) and the satellite-based Chl-a
201 concentration extracted along the VPR transect reveals similarity between two variables
202 (Fig. 4d). Both VPR fluorescence and MODIS Chl-a were highest near the frontal region
203 between the two eddies. Clearly, the satellite observations do not reflect the deeper
204 structure of the fluorescence distribution (Fig. 4c) which results in local maxima of
205 depth-integrated fluorescence located at the center of Eddy 1 and at the frontal boundary
206 in between the two eddies (Fig. 4d).

207

208 2.3 CTD transects

209 On January 25-26, 2012, two CTD transects were conducted: one along the edge
210 (within several kilometers) of the RIS, and one normal to it (Fig. 3). In general, waters
211 along the RIS tended to be colder and fresher than those to the north (Fig. 5). However,
212 there was considerable variability in properties along the ice shelf. At station 62, there
213 was a cold and fresh layer extending to nearly 150m, with patchy fluorescence
214 throughout that interval. This vertical structure is reminiscent of that observed in the
215 interiors of Eddies 1 and 2, with very similar temperature and salinity characteristics.

216

217 3. Model configuration

218 The Regional Ocean Modeling System (ROMS, Haidvogel et al., 2008; Shchepetkin
219 and McWilliams, 2005) is used in this study. ROMS is a free-surface, hydrostatic,
220 primitive-equation model that employs split-explicit separation of fast barotropic and
221 slow baroclinic modes and vertically stretched terrain-following coordinates. An ice shelf
222 module is coupled with the ocean model (Dinniman et al., 2011; Stern et al., 2013). The
223 K -profile parameterization (KPP) turbulence closure scheme (Large et al., 1994) is
224 applied to compute both momentum and tracer vertical mixing. The KPP scheme is

225 modified according to Dinniman et al. (2003), which prevents the mixed layer from
226 unrealistic shallowing during stratified conditions. Sensitivity tests show that altering
227 values for horizontal diffusivity within reasonable ranges have limited impact on the
228 major conclusions herein (Appendix A). Quadratic drag is used to compute the frictional
229 force on water in contact with the bottom and the ice shelf. The model also includes
230 mechanical and thermodynamic interactions between the floating ice shelf and water
231 cavity underneath (Holland and Jenkins, 1999; Dinniman et al., 2011; Stern et al., 2013).
232 A brief description on the parameterization of the ice shelf basal melting is provided in
233 Appendix B. Interested readers are referred to Dinniman et al. (2011) for additional
234 details of the model.

235

236 3.1 Model grid and ice shelf

237 Our idealized 2-D and 3-D models of the RIS utilize the same cross-shelf geometry,
238 configured to mimic the average bottom elevation and ice shelf draft in Bedmap2
239 (Fretwell et al., 2013) data for the area of interest (Fig. 6). This configuration is similar to
240 that used in another idealized modeling study (Gwyther et al., 2015). It reflects a
241 representative average of the many years the data that were collected to form Bedmap2,
242 rather than the specific details of the geometry present in January 2012 when the eddies
243 of interest were observed. Both our 2D and 3D models have 100 vertical layers, and
244 horizontal grid resolution of 500 m in the along-ice shelf and cross- ice shelf direction
245 (referred to as the X- and Y-directions, respectively). The horizontal resolution is
246 approximately one order of magnitude smaller than the first baroclinic Rossby radius of
247 deformation, thus making it suitable for simulating eddy processes at an ice shelf front
248 (Årthun et al., 2013). The bottom is flat with a depth of 600 m. The model domains span
249 500 km in the cross- ice shelf direction in order to minimize impacts of the open offshore
250 boundary on the processes of interest near the ice shelf. The 3-D model domain spans 100
251 km in the along- ice shelf direction. See Appendix B for additional information pertaining

252 to accuracy of the pressure gradient calculation in this particular geometry.

253

254 3.2 Initial and boundary conditions

255 Both initial and boundary conditions (Fig.6) are spatially uniform based on the
256 vertical temperature and salinity profiles from CTD station 58, the most offshore station
257 for the RIS CTD survey (Fig. 5). This site was chosen to reflect ambient conditions,
258 outside of the immediate influence of the ice shelf. Initial velocities and sea level
259 elevations are set to zero. The selection of the initial condition is *ad hoc*, as the
260 hydrographic conditions near the edge of the ice shelf were not sampled extensively.
261 Some of the uncertainties associated with the initial condition are assessed in section 6.

262 A closed wall is imposed on the southern boundaries of the model domains. In the
263 north, open boundary conditions are applied to tracers following the method of
264 Marchesiello et al. (2001), with the external values provided by CTD station data. At the
265 open northern boundary of both models, a 20-point sponge layer provides enhanced
266 viscosity and diffusivity to suppress numerical noise generated by wave reflection. The
267 2-D model actually includes six grid points in the along- ice shelf direction, but periodic
268 boundary conditions yield a solution that is effectively 2-D. Periodic boundaries are also
269 used in the 3-D model, but its 100 km extent in the along- ice shelf direction allows
270 energetic mesoscale flows to develop. No tidal forcing is included in the model.

271

272 3.3 Surface forcing

273 Wind forcing is from the Antarctic meteorological station VITO on the Ross Ice Shelf
274 (Fig. 1). The three hourly wind speed from VITO is converted to wind stress based on the
275 formulation of Large and Pond (1981), and the wind forcing is assumed to be spatially
276 uniform over the entire model domain. We compared the VITO record (Fig. 7) with
277 shipboard wind measurements during the time period when the RIS area was being
278 sampled (January 23-26). Both sources indicated southerly flow during that period,

279 although the winds measured at sea were at times up to 50% stronger (not shown). This
280 comparison confirms the VITO winds are appropriate forcing for the model simulations;
281 the impact of the apparent increase in winds over the ocean is addressed in sensitivity
282 experiments described in Section 5. There is no surface flux of fresh water. A constant
283 surface net heat flux of 35 W m^{-2} into the ocean is specified, which is the mean value for
284 the month of January from the 3-D model simulations of the Ross Sea described in
285 Dinniman et al. (2011). As we are simulating summer ice-free conditions, the sea ice
286 module available in ROMS is turned off.

287

288 3.4 Ross Ice Shelf edge roughness in the 3-D model

289 To implement realistic roughness in the edge of the RIS, we first digitized the edge
290 from the Bedmap2 ice thickness (<http://nora.nerc.ac.uk/501469/>). Second, those
291 roughness elements were projected onto the straight ice shelf edge in our idealized
292 geometry. The characteristic ice shelf edge roughness length scales of 5-20 km (Fig. 8c-f)
293 are well resolved by the 1 km resolution Bedmap2 database. These roughness scales are not
294 inconsistent with those present in the MODIS imagery (Figs. 2 and 3). This suggests that
295 roughness derived from Bedmap2 is suitably realistic, despite being derived from a
296 longer-term average rather than an instantaneous snapshot.

297

298 4. Numerical simulation of RIS eddies

299 Both satellite imagery and the *in situ* VPR observations documented the presence of
300 the cold and fresh eddies near the RIS edge. It is therefore of interest to explore the
301 generation mechanisms responsible for their formation. To do this, we design three
302 experiments evaluating the relative importance of three factors: ice shelf roughness, basal
303 melting, and surface wind stress (Table 1). Except where otherwise noted, the 3-D
304 simulations are run for 25 days.

305 The baseline case includes a straight ice shelf, wind forcing, and basal melting (run

306 SIS+WIND+BM). Our basal melt rate for the ice shelf front (between 6-16 km of the ice
307 shelf edge) in the model is $1.0\pm 0.4 \text{ m yr}^{-1}$, similar to the estimate by Arzeno et al. (2014)
308 using mooring observations ($1.2\pm 0.5 \text{ m yr}^{-1}$). The estimated basal melt rate between 1-5
309 km of the ice shelf edge from our model is $3.2\pm 0.9 \text{ m yr}^{-1}$, and is comparable to the estimate
310 of Horgan et al. (2011) for that region based on satellite altimetry ($\sim 2.1\pm 0.9 \text{ m yr}^{-1}$).

311 A cold and fresh boundary layer forms at the edge of the ice shelf due to basal
312 melting, generating a baroclinic jet (Fig. 8 a, b), a feature similar to that described by
313 Niebauer (1982) for a marginal sea ice edge. This is also consistent with a westward
314 coastal jet found near the RIS front (Jacobs et al., 1970; Keys et al., 1990). Variations in
315 surface velocity in the interior of the model domain away from the baroclinic jet at the
316 edge of the ice shelf are driven by wind forcing. In this experiment, we see no evidence
317 for generation of the types of mesoscale structures we observed (Figs. 2 and 3), even
318 when the model was run out for an additional 60 days (not shown).

319 When the straight ice shelf is replaced with an irregular one (run IIS+WIND+BM),
320 mesoscale instabilities develop in the boundary current, shedding cold and fresh eddies
321 into the interior (Fig. 8 c, d). The eddies are larger than the spatial scale of ice shelf
322 irregularities, and therefore the eddy structure is not expected to be set by the ice shelf
323 roughness. Indeed, we expect the eddy scale to be related to the Rossby radius of
324 deformation. We performed a sensitivity experiment in which the amplitude of the
325 roughness perturbations was reduced to 1/8 of the realistic case, and found similar sized
326 eddies were created on the same time scales (not shown). This suggests that our results are
327 not particularly sensitive to the details of the specified roughness.

328 To quantify the importance of wind forcing, the experiment was repeated with wind
329 forcing turned off (run IIS+BM). Instability in the boundary current persists (Fig. 8 e, f),
330 generating cold and fresh eddies similar those present in run IIS+WIND+BM (Fig. 8 c, d).
331 Thus wind forcing is not necessary for eddy formation, although it does make the
332 resulting eddies more energetic (Cf. Figs. 8c, d and 8e, f), with a domain-wide eddy

333 kinetic energy 60% larger than the no-wind case at model day 25. Additional experiments
334 were conducted to determine the degree to which the results were sensitive to the phasing
335 of the wind fluctuations. This was accomplished by starting the simulations at different
336 times during the wind record. Although the detailed evolution of the eddy field differed as
337 a result of these variations in forcing, the qualitative behavior was unchanged.

338 We note that temperatures in these simulations are higher than observed (Cf. Figs. 3,
339 8). The model is initialized with temperature and salinity profiles observed during the
340 field survey (January 25), and we apply a constant surface heat flux (35 W m^{-2})
341 throughout the simulations. It is therefore not surprising that the simulated temperature is
342 higher than observed. Our idealized simulations are aimed at understanding eddy
343 formation mechanisms, rather than hindcasting the specifics of the observed conditions.

344 Pawlak and McCready (2002) conducted laboratory experiments to study the
345 instabilities associated with oscillatory flow. Their results showed that oscillatory flow
346 along an irregular coastline can change streamlines and vorticity, thus providing a
347 mechanism for transferring anomalies from the boundary to the interior of the flow. The
348 instability and eddies are further found to be linked to the along-shore flow length scale
349 and roughness length scale, a finding consistent with numerical simulations of Signell
350 and Geyer (1991). With a rougher ice edge with smaller length scale, a stronger
351 eddy-driven flow is present. In our case, a similar mechanism exists. The formation of
352 cold and fresh anomalies due to basal melting first generates an along-shelf flow. The
353 resulting baroclinic current is perturbed by irregular ice shelf edge, triggering instability
354 that forms eddies, which carry the cold and fresh anomalies offshore to the open ocean.
355 The inclusion of wind forcing, though, can modulate the instabilities through
356 wind-induced oscillations in cross-ice shelf flow, thus further changing the timing and
357 detailed structure of eddies. Chu (1987) studied the fast ice-ocean interaction, and found
358 that even without any prescribed external forcing, the most unstable vertical wave mode
359 can be excited by curvatures in the ice edge, which is also consistent with our conclusion

360 here.

361 To compare with the observed eddies that are separated from the ice shelf on January
362 25, we sample a cross-section of one of the eddies simulated in run IIS+WIND+BM (Fig.
363 8cd). It reveals a lens of cold and fresh water is present in the upper 35 m (Fig. 9).

364 Although the hydrographic structure of the simulated eddy is qualitatively similar to
365 observations, the thickness of the lens is much less than indicated by the VPR survey (Fig.
366 4). Mechanisms for thickening the lens of cold and fresh water are the subject of the next
367 section.

368

369 **5. 2-D model simulations**

370 We showed that the cold eddy formation is facilitated by ice shelf roughness and
371 basal melting. Since the thick lenses are observed both within the mesoscale RIS eddies
372 as well as at the RIS edge where the eddies originate, it would therefore be of interest to
373 understand what controls the surface lens thickening at the edge of the ice shelf.

374 For this purpose, a series of 2-D model sensitivity experiments are carried out with
375 simulations running for 30 days (Table 2). In the first experiment (run WIND), the model
376 is forced by wind only. A strong downwelling-favorable wind event during January 22-28
377 (Fig. 7) forms a thick layer of relatively warm and fresh waters adjacent to the RIS,
378 composed of surface waters drawn in from offshore and downwelled at the ice edge (Fig.
379 10 a, f, k). Although the salinity of the downwelled fluid is low, it is not as low as
380 observed (Fig. 5), suggesting glacial melt is involved in freshening of the waters adjacent
381 to the RIS. In the second case (run BM), the wind forcing is turned off and basal melting
382 is turned on. Buoyant convection of meltwater from the underside of the ice shelf leads to
383 a cold and fresh layer adjacent to the RIS that depresses the pycnocline by a few tens of
384 meters (Fig. 10 b, g, l). Offshore of this boundary layer, strong stratification develops in
385 surface waters owing to the surface heat flux and lack of turbulent kinetic energy input
386 from the wind. In the third case (run WIND+BM), the combination of wind forcing and
387 basal melt creates a thick (~65 m) lens of cold and fresh water adjacent to the ice shelf

388 (Fig. 10 c, h, m). With wind forcing restored, stratification of the waters north of the ice
389 shelf is similar to that of the first experiment (Cf. Fig. 10 a, f, k and c, h, m).

390 Although run WIND+BM generates a layer of cold and fresh water reminiscent of
391 that observed near the ice shelf (Fig. 5), it is not as thick. Two more sensitivity
392 experiments are conducted to assess whether or not this discrepancy between the
393 simulated and observed distributions could be explained by differences in the forcing and
394 initial conditions. First, the wind stress was increased by 50% (run HWIND+BM, Fig. 10
395 d, i, n). This causes a modest deepening of the cold fresh layer, from ~65 m in run
396 WIND+BM to ~75 m in run HWIND+BM. Second, as the initial condition is rather *ad*
397 *hoc* due to limited observations available near ice shelf edge, the temperature, salinity,
398 and density fields in the initial condition were made constant below 50 m, with the
399 observed wind forcing applied (run WIND+BM+WS, Cf. Fig.10 e, j, o and c, h, m). This
400 reduction in the stratification allows the cold and fresh layer to deepen to 150 m (below
401 the vertical interval shown in Fig. 10). By reducing the buoyancy Richardson number, the
402 same input of turbulent kinetic energy can homogenize a thicker layer of the upper water
403 column (Abarbanel et al., 1984), thus providing more deepening of the mixed layer by
404 the same amount of surface stress (Trowbridge, 1992).

405

406 **6. Discussion**

407 The 3-D numerical experiments highlight the role of irregularities in the geometry
408 of the ice shelf edge in stimulating eddy formation. The propagation of these eddies away
409 from the RIS can facilitate the lateral transport of glacial meltwater and *P. antarctica*
410 blooms into the interior of the Ross Sea. Our results are consistent with the previous
411 findings by Chu (1987), which showed in a semi-analytical framework that unstable
412 wave modes can be excited by along-ice shelf curvatures. This mechanism of eddy
413 formation is also similar to that found in tidal regimes. Both numerical models (Signell
414 and Geyer, 1992) and laboratory observations (Pawlak and MacCready, 2002), illustrate
415 how irregularities in geometry such as ridges and/or headlands can facilitate flow

416 separation, causing vortices to be injected into the ocean interior. The origin of the cold
417 and fresh near-surface layer adjacent to the RIS can be attributed to basal melting, as
418 evidenced by comparison of the 2-D experiments with and without this effect. However,
419 the properties of this lens may be influenced by other processes not simulated by the
420 model. For example, formation of frazil ice can make the ice shelf water even more
421 buoyant (Jenkins and Bombosch, 1995; Smedsrud and Jenkins, 2004). Moreover, along-
422 ice shelf variability in the RIS plume may be driven by a host of factors, including spatial
423 variations in the cavity geometry, atmospheric forcing, and basal melting rate.

424 Downwelling-favorable winds were shown to be an important agent of thickening the
425 near-surface lens of cold and fresh water at the edge of the ice shelf. In order to ascertain
426 the degree to which such conditions may prevail at the RIS during summertime, we
427 compute the cumulative upwelling index for each January during the period 2010-2014.
428 First, the upwelling index (UI) is computed according to $UI = \frac{\tau_x}{\rho f}$ (i.e., the offshore
429 component of the Ekman transport) following the method of *Schwing et al.* (1996), where
430 τ_x is the alongshore component of wind stress calculated using the Large and Pond (1981)
431 scheme, and f is the local Coriolis parameter. Positive (negative) UI represents upwelling
432 (downwelling) favorable wind conditions. The cumulative UI (CUI) is then computed by
433 integrating the resulting UI over time (i.e., $CUI = \int UI dt$) between January 1 and January
434 31 of each year. The slope of CUI is particularly informative, in that the most
435 downwelling-favorable wind conditions are represented by the steepest descending trend
436 shown in CUI. In contrast, a rising trend in CUI indicates that upwelling-favorable wind
437 (negative UI) becomes more dominant.

438 All Januaries in the time period examined exhibited downwelling-favorable wind
439 conditions (Fig. 11). However, there is significant interannual variability—and our
440 observations were collected during a time period when the downwelling-favorable aspect
441 of the wind was relatively modest. We therefore conclude that wind-forced thickening of

442 the cold and fresh layer may be a frequent occurrence in this regime. However, other
443 mechanisms such as variations in the basal melting rate could be as important or perhaps
444 even more so.

445

446 **7. Summary and Conclusions**

447 *In situ* observations along with numerical model simulations were used to investigate
448 the dynamics of cold and fresh eddies near the edge of the Ross Ice Shelf that contained
449 high phytoplankton biomass, dominated by *P. antarctica*.

450 Idealized 3-D model simulations were able to generate eddies near the RIS with
451 properties similar to those observed. Sensitivity experiments showed that basal melting
452 can produce a cold and fresh plume adjacent to the RIS, which accelerates a baroclinic
453 current. In the presence of irregularities in the edge of the ice shelf, that current becomes
454 unstable and sheds eddies with the cold and fresh water mass properties of the plume.

455 The plume is consistent with previous findings of Niebauer (1983), and the eddy
456 formation mechanism is similar to results from previous numerical simulations (Chu et
457 al., 1987; Signell and Geyer, 1992) and laboratory experiments (Pawlak and McCready,
458 2002). However, in our simulations the cold and fresh lenses were quantitatively
459 shallower than observed by VPR (35 m vs. 80 m). Idealized 2-D model simulations were
460 then used to investigate the processes that can deepen the cold and fresh surface layer
461 adjacent to the RIS. Wind-induced downwelling can deepen the layer, and the magnitude
462 of this effect depends on the strength of the wind and the underlying
463 stratification—neither of which are particularly well constrained by available data.

464 Sensitivity experiments using the 2-D model document that plausible perturbations to the
465 wind stress and stratification can result in formation of a cold and fresh layer with a
466 vertical extent similar to that observed near the edge of the RIS and in the RIS eddies. A
467 follow-up 3-D simulation with reduced stratification produces thicker lenses within the
468 simulated eddies (not shown). However, we note that the observations document
469 substantial along-ice shelf variability in the density structure. Thus, the thickness of the

470 cold and fresh layer entrained into RIS eddies will vary depending on ambient conditions
471 present at the time of eddy formation. Although our idealized 3-D simulations did not
472 produce eddies with lenses as thick as those observed, we expect that a model with more
473 realistic along- ice shelf variability in water masses, subsurface ice shelf-roughness,
474 stratification, and surface forcing (wind and heat flux) would do just that. Lateral fluxes
475 associated with these eddies may be important in transporting physical, chemical and
476 biological properties from the RIS into the interior Ross Sea.
477

478 **Acknowledgements**

479 The data used in this paper are archived at the Biological and Chemical
480 Oceanography Data Management Office: <http://www.bco-dmo.org/project/2155>.
481 Support of this research by the National Science Foundation's United States Antarctic
482 Program is gratefully acknowledged. We thank the officers, crew, and technical personnel
483 on board the R/V *Nathaniel B. Palmer* for their outstanding support during our seagoing
484 operations. O. Kosnyrev and V. Kosnyrev provided assistance with data analysis and
485 figure preparation. YL thanks Drs. John Trowbridge, Jim Ledwell, and Weifeng Gordon
486 Zhang for useful discussions on ocean mixing. YL also thanks Drs. Kenneth Brink and
487 Steve Lentz for insights into instability processes that improved interpretation of the
488 model results. We would also like to acknowledge high-performance computing
489 [Yellowstone (ark:/85065/d7wd3xhc)] provided by NCAR's Computational and
490 Information Systems Laboratory, sponsored by the National Science Foundation. MODIS
491 level 2 satellite data and diffusion attenuation coefficient for downwelling irradiance at
492 490 nm were made publicly available by NASA Goddard Space Flight Center
493 (<http://modis.gsfc.nasa.gov/data/>). Complete wind speed data in 2010-2014 at station
494 VITO were kindly provided by Carol Costanza (carol.costanza@ssec.wisc.edu) at
495 University of Wisconsin with addition input from Dr. Douglas MacAyeal
496 (drm7@uchicago.edu) at University of Chicago. Bedmap2 data is archived by British
497 Antarctic Survey (<http://nora.nerc.ac.uk/501469/>). YL is supported by the Postdoctoral
498 Scholarship Program at Woods Hole Oceanographic Institution, with funding provided by
499 the Dr. George D. Grice Postdoctoral Scholarship.

500

501 **References**

- 502 Abarbanel, H. D., Holm, D. D., Marsden, J. E., and Ratiu, T., 1984. Richardson number
503 criterion for the nonlinear stability of three-dimensional stratified flow. *Phys. Rev.*
504 *Lett.*, 52, 2352.
- 505 Arrigo, K. R., Worthen, D., Schnell, A., and Lizotte, M. P., 1998, Primary production in
506 Southern Ocean waters. *J. Geophys. Res.*, 103, 15587-15600.
- 507 Arrigo, K.R., Worthen, D.L. and Robinson, D.H., 2003. A coupled ocean - ecosystem

508 model of the Ross Sea: 2. Iron regulation of phytoplankton taxonomic variability and
509 primary production. *J. Geophys. Res. Oceans*, 108(C7).

510 Arrigo, K. R., van Dijken, G. L., and Strong, A. L. 2015, Environmental controls of
511 marine productivity hot spots around Antarctica. *J. Geophys. Res. Oceans*,
512 10.1002/2015JC010888.

513 Årthun, M., Holland, P. R., Nicholls, K. W., & Feltham, D. L., 2013. Eddy-Driven
514 Exchange between the Open Ocean and a Sub-Ice Shelf Cavity. *J. Phys. Oceanogr.*,
515 43-11, 2372-2387.

516 Arzeno, I. B., R.C. Beardsley, R. Limeburner, B. Owens, L. Padman, S. R. Springer, C. L.
517 Stewart, and M. JM., Williams, 2014. Ocean variability contributing to basal melt
518 rate near the ice front of Ross Ice Shelf, Antarctica. *J. Geophys. Res. Oceans*, 119, 7:
519 4214-4233.

520 Carder, K. L., Chen, F. R., Cannizzaro, J. P., Campbell, J. W., and Mitchell, B. G., 2004,
521 Performance of the MODIS semi-analytical ocean color algorithm for chlorophyll-a.
522 *Adv. Space Res.*, 33, 1152-1159.

523 Clark, D. K., 1997. Algorithm theoretical basis document–Bio-optical algorithms, Case I
524 waters, MODIS algorithm theoretical basis document 18, Version 1.2, available from:
525 http://modis.gsfc.nasa.gov/data/atbd/atbd_mod18.

526 Clarke, A. J., 1978. On wind-driven quasi-geostrophic water movements near fast-ice
527 edges. *Deep-Sea Res.*, 25, 41-51.

528 Chu, P., 1987. An air-sea feedback mechanism for quasi-geostrophic water movement
529 near a fast shelf-ice edge with a small curvature, *Chinese J. Atmos. Sci.* 11, 31-42.

530 Comiso, J.C., McClain, C.R., Sullivan, C.W., Ryan, J.P., Leonard, C.L., 1993. Coastal
531 Zone Color Scanner pigment concentrations in the Southern Ocean and relationships
532 to geophysical surface features. *J. Geophys. Res.*, 98, 2419-2451.

533 Cushman-Roisin, B., Tang, B., & Chassignet, E. P., 1990. Westward motion of mesoscale
534 eddies. *J. Phys. Oceanogr.*, 20, 758-768.

535 Davis, C. S., Gallager, S. M., Berman, M. S., Haury, L. R., and Strickler, J. R. ,1992. The
536 video plankton recorder (VPR): design and initial results. *Arch. Hydrobiol. Beih*, 36,
537 67-81.

538 Depoorter, M. A., Bamber, J. L., Griggs, J. A., Lenaerts, J. T. M., Ligtenberg, S. R. M.,
539 van den Broeke, M. R., and Moholdt, G. ,2013. Calving fluxes and basal melt rates
540 of Antarctic ice shelves. *Nature*, 502, 89-92.

541 Dinniman, M.S., J.M. Klinck and W.O. Smith, Jr., 2003. Cross-shelf exchange in a model
542 of the Ross Sea circulation and biogeochemistry, *Deep-Sea Res. II*, 50, 3103-3120.

543 Dinniman, M.S. and J.M. Klinck, 2004. A model study of circulation and cross-shelf
544 exchange on the west Antarctic Peninsula continental shelf, *Deep-Sea Res. II*, 51,
545 2003-2022.

546 Dinniman, M. S., J. M. Klinck, and W. O. Smith Jr., 2007. The influence of sea ice cover
547 and icebergs on circulation and water mass formation in a numerical circulation
548 model of the Ross Sea, Antarctica. *J. Geophys. Res.*, 112, C11013,

549 doi:10.1029/2006JC004036.

550 Dinniman, M.S., J.M. Klinck and W.O. Smith, Jr, 2011. A model study of Circumpolar
551 Deep Water on the West Antarctic Peninsula and Ross Sea continental shelves.
552 *Deep-Sea Res. II*, 58, 1508-1523, doi: 10.1016/j.dsr2.2010.11.013

553 Dinniman, M.S., J.M. Klinck and E.E. Hofmann, 2012. Sensitivity of Circumpolar Deep
554 Water transport and ice shelf basal melt along the west Antarctic Peninsula to
555 changes in the winds. *J. Clim.*, 25, 4799-4816.

556 Dumont, D., Gratton, and T. Arbetter, 2010. Modeling Wind-Driven Circulation and
557 Landfast Ice-Edge Processes during Polynya Events in Northern Baffin Bay. *J. Phys.*
558 *Oceanogr.*, 40, 1356–1372. doi:10.1175/2010JPO4292.1

559 Erofeeva, S. Y., Padman, L., & Egbert, G. (2005). Assimilation of ship-mounted ADCP
560 data for barotropic tides: Application to the Ross Sea. *Journal of Atmospheric and*
561 *Oceanic Technology*, 22(6), 721-734.

562 Falkowski, P. G., and Kolber, Z. ,1995. Variations in chlorophyll fluorescence yields in
563 phytoplankton in the world oceans. *Funct. Plant Biol.*, 22, 341-355.

564 Foldvik, A., & Kvinge, T. ,1974. Conditional instability of sea water at the freezing point.
565 *Deep-Sea Res.*, 21, 3, 169-174.

566 Foster, T. D., 1983. The temperature and salinity fine structure of the ocean under the
567 Ross Ice Shelf. *J. Geophys. Res.*, 88, 2556-2564.

568 Fretwell, P., et al. (2013). Bedmap2: improved ice bed, surface and thickness datasets for
569 Antarctica. *The Cryosphere*, 7.1.

570 Galton-Fenzi, B.K., 2009. Modelling Ice-Shelf/Ocean Interaction. Ph.D. thesis,
571 University of Tasmania, 151 pp.

572 Gerringa, L. J. et al., 2012. Iron from melting glaciers fuels the phytoplankton blooms in
573 Amundsen Sea (Southern Ocean): Iron biogeochemistry. *Deep-Sea Res. II*, 71,
574 16-31.

575 Gilmour, A. E., 1979. Ross ice shelf sea temperatures. *Science*, 203(4379), 438-439.

576 Gordon, A.L., A.H. Orsi, R. Muench, B.A. Huber, E. Zambianchi, and M. Visbeck, 2009.
577 Western Ross Sea continental slope gravity currents. *Deep-Sea Res. II*, 56, 796-817.

578 Goring, D.G., and Pyne, A., 2003. Observations of sea level variability in Ross Sea,
579 Antarctica. *NZ J. Mar. Freshwater Res.*, 37: 241–249.

580 Gwyther, D. E., Galton-Fenzi, B. K., Dinniman, M. S., Roberts, J. L., & Hunter, J. R. ,
581 2015. The effect of basal friction on melting and freezing in ice shelf–ocean models.
582 *Ocean Modell.*, 95, 38-52.

583 Haidvogel, D. B., Arango, H., Budgell, W. P., Cornuelle, B. D., Curchitser, E., Di
584 Lorenzo, E., ... and Wilkin, J. ,2008. Ocean forecasting in terrain-following
585 coordinates: Formulation and skill assessment of the Regional Ocean Modeling
586 System. *J. Comput. Phys.*, 227, 3595-3624.

587 Häkkinen, S., 1986: Coupled ice-ocean dynamics in the marginal ice zones,
588 upwelling/downwelling and eddy generation. *J. Geophysical Research*, 91, 819–832.

589 Holland, D. M., and Jenkins, A., 1999. Modeling thermodynamic ice-ocean interactions

590 at the base of an ice shelf. *J. Phys. Oceanogr.*, 29, 1787-1800.

591 Horgan, H.J., R.T. Walker, S. Anandakrishnan, and R.B. Alley, 2011. Surface elevation
592 changes at the front of the Ross Ice Shelf: Implications for basal melting. *J. Geophys.*
593 *Res.*, 116, C02005.

594 Jacobs, S. S., Amos, A. F., & Bruchhausen, P. M., 1970. Ross Sea oceanography and
595 Antarctic bottom water formation. *Deep-Sea Res.*, 17, 6, 935-962.

596 Jacobs, S. S., Gordon, A. L., and Ardai, J. L., 1979. Circulation and melting beneath the
597 Ross Ice Shelf, *Science*, 203, 439-443.

598 Jacobs, S.S., Fairbanks, R.G., and Horibe, Y., 1985. Origin and evolution of water masses
599 near the Antarctic continental margin: evidence from $H_2^{18}O/H_2^{16}O$ ratios in seawater.
600 in: *Oceanology of the Antarctic Continental Shelf* (S. Jacobs, ed.), Antarct. Res, Ser.,
601 American Geophysical Union, Washington D.C., 43, 59-85.

602 Jacobs, S. S. (1992). Is the Antarctic ice sheet growing? *Nature*, 360, 29-33.

603 Jacobs, S. S., Hellmer, H. H., & Jenkins, A. ,1996. Antarctic ice sheet melting in the
604 Southeast Pacific. *Geophys. Res. Lett.*, 23, 957-960.

605 Jacobs, S. S., Jenkins, A., Giulivi, C. F., and Dutrieux, P. ,2011. Stronger ocean
606 circulation and increased melting under Pine Island Glacier ice shelf. *Nature Geosci.*,
607 4, 519-523.

608 Jenkins, A., and Doake, C. S. M., 1991. Ice-ocean interaction on Ronne Ice Shelf,
609 Antarctica. *J. Geophys. Res. Oceans*, 96, 791-813.

610 Jenkins, A., and Bombosch, A., 1995. Modeling the effects of frazil ice crystals on the
611 dynamics and thermodynamics of ice shelf water plumes. *J. Geophys. Res. Oceans*,
612 100, 6967-6981.

613 Keys, H. J., Jacobs, S. S., and Barnett, D., 1990. The calving and drift of iceberg B-9 in
614 the Ross Sea, Antarctica. *Antarctic Sci.*, 2, 243-257.

615 Klinck, J. M., Hofmann, E. E., Beardsley, R. C., Salihoglu, B., and Howard, S., 2004.
616 Water-mass properties and circulation on the west Antarctic Peninsula Continental
617 Shelf in austral fall and winter 2001. *Deep-Sea Res. II*, 51, 1925-1946.

618 Klinck, J. M., and M. S. Dinniman, 2010. Exchange across the shelf break at high
619 southern latitudes. *Ocean Sci.*, 6, 513–524.

620 Krauss, E.B., Turner, J.S., 1967. A one-dimensional model of the seasonal thermocline.
621 *Tellus* 19, 98–105.

622 Large, W. G., and Pond, S., 1981. Open ocean momentum flux measurements in
623 moderate to strong winds. *J. Phys. Oceanogr.*, 11, 324-336.

624 Large, W. G., McWilliams, J. C., and Doney, S. C., 1994. Oceanic vertical mixing: A
625 review and a model with a nonlocal boundary layer parameterization. *Rev. Geophys.*,
626 32, 363-404.

627 Losch. M., 2008. Modeling ice shelf cavities in a z coordinate ocean general circulation
628 model. *J. Geophys. Res. Oceans*, 113, C08043.

629 MacAyeal, D. R., 1984. Thermohaline circulation below the Ross Ice Shelf: A
630 consequence of tidally induced vertical mixing and basal melting. *J. Geophys. Res.*

631 Oceans, 89, 597-606.

632 MacAyeal, D. R., 1985. Tidal rectification below the Ross Ice Shelf, Antarctica. *Antarct.*
633 *Res. Ser.*, 43, 109-132.

634 Makinson, K., Schröder, M., & Østerhus, S., 2006. Effect of critical latitude and seasonal
635 stratification on tidal current profiles along Ronne Ice Front, Antarctica. *J. Geophys.*
636 *Res.*, Oceans, 111, C03022.

637 Marchesiello, P., J.C. McWilliams, and A.F. Shchepetkin, 2001. Open boundary
638 conditions for long-term integration of regional oceanic models. *Ocean Modell.*, 3,
639 1-20.

640 Martin, J. H., 1990. Glacial - interglacial CO₂ change: The iron hypothesis.
641 *Paleoceanogr.*, 5(1), 1-13.

642 McGillicuddy, D.J., Sedwick, P.N., Dinniman, M.S., Arrigo, K.R., Bibby, T.S., Greenan,
643 B.J.W., Hofmann, E.E., Klinck, J.M., Smith, W.O., Mack, S.L., Marsay, C.M., Sohst,
644 B.M., and G.L. van Dijken, 2015. Iron supply and demand in an Antarctic shelf
645 ecosystem, *Geophys. Res. Lett.*, 42, 8088–8097.

646 Mellor, G. L., and Blumberg, A. F., 1985. Modeling vertical and horizontal diffusivities
647 with the sigma coordinate system. *Mon. Weather Rev.*, 113, 1379-1383.

648 Nicholls, K. W., Padman, L., Schröder, M., Woodgate, R. A., Jenkins, A., & Østerhus, S.,
649 2003. Water mass modification over the continental shelf north of Ronne Ice Shelf,
650 Antarctica. *J. Geophys. Res. Oceans*, 108, 3260.

651 Niiler, P.P., Kraus, E.B., 1977. One-dimensional models of the Upper Ocean. In: Krauss,
652 E.B. (Ed.), *Modeling and Prediction of the Upper Layers of the Ocean*. Pergamon,
653 New York, pp. 143–172.

654 Niebauer, H. J., 1982. Wind and melt driven circulation in a marginal sea ice edge frontal
655 system: a numerical model. *Cont. Shelf Res.*, 1, 49-98.

656 Orsi, A.H., Smethie Jr., W.M., and Bullister, J.L., 2002. On the total input of Antarctic
657 Waters to the Deep Ocean: a preliminary estimate from chlorofluorocarbon
658 measurements. *J. Geophys. Res. Oceans*, 107, 3122.

659 Orsi, A.H. and Wiederwohl, C.L., 2009. A recount of Ross Sea waters. *Deep Sea*
660 *Research II*, 56, 13-14, doi:10.1016/j.dsr2.2008.10.033.Pawlak, G., and MacCready,
661 P., 2002. Oscillatory flow across an irregular boundary. *J. Geophys. Res. Oceans*, 107,
662 4-1.

663 Pawlak, G., & MacCready, P. 2002. Oscillatory flow across an irregular boundary. *J.*
664 *Geophys. Res. Oceans*, 107(C5).

665 Pritchard, H. D., Ligtenberg, S. R. M., Fricker, H. A., Vaughan, D. G., Van den Broeke,
666 M. R., and Padman, L., 2012. Antarctic ice-sheet loss driven by basal melting of ice
667 shelves. *Nature*, 484, 502-505.

668 Rignot, E., Jacobs, S., Mouginot, J., and Scheuchl, B., 2013. Ice-shelf melting around
669 *Antarct. Science*, 341, 266-270.

670 Schwing, F. B., O'Farrell, M., Steger, J. M., and Baltz, K., 1996. Coastal Upwelling
671 indices west coast of North America. *NOAA Tech. Rep.*, NMFS SWFSC, 231, 144p.

- 672 Shchepetkin, A.F., McWilliams, J.C., 1998. Quasi-monotone advection schemes based on
673 explicit locally adaptive dissipation. *Mon. Weather Rev.*, 126, 1541–1580.
- 674 Shchepetkin, A. F., & McWilliams, J. C., 2003. A method for computing horizontal
675 pressure-gradient force in an oceanic model with a nonaligned vertical coordinate. *J.*
676 *Geophys. Res. Oceans*, 108, 1-33.
- 677 Shchepetkin, A. F., and McWilliams, J. C., 2005. The regional oceanic modeling system
678 (ROMS): a split-explicit, free-surface, topography-following-coordinate oceanic
679 model. *Ocean Modell.* 9, 347-404.
- 680 Sedwick, P. N., G. R. DiTullio, and D. J. Mackey (2000), Iron and manganese in the Ross
681 Sea, Antarctica: Seasonal iron limitation in Antarctic Shelf Waters, *J. Geophys. Res.*
682 *Oceans*, 105(C5), 11321-11336.
- 683 Signell, R., P., and W. R., Geyer, 1991. Transient eddy formation around headlands. *J.*
684 *Geophys. Res. Oceans*, 96: 2561-2575.
- 685 Smedsrud, L. H., and Jenkins, A., 2004. Frazil ice formation in an ice shelf water plume.
686 *J. Geophys. Res. Oceans*, 109, C03025.
- 687 Smethie Jr., W.M. and Jacobs, S.S., 2005. Circulation and melting under the Ross Ice
688 Shelf: estimates from evolving CFC, salinity and temperature fields in the Ross Sea.
689 *Deep-Sea Res. I*, 52, 959-978.
- 690 Smith Jr, W. O., and D. J. McGillicuddy et al., Ghost colonies of *Phaeocystis*: distribution
691 and abundance in the Ross Sea, submitted, this issue.
- 692 Smith Jr, W. O., Ainley, D. G., Arrigo, K. R., & Dinniman, M. S. ,2014. The
693 oceanography and ecology of the Ross Sea. *Ann. Rev. of Mar. Sci.*, 6, 469-487.
- 694 Stern, A. A., Dinniman, M. S., Zagorodnov, V., Tyler, S. W., and Holland, D. M. 2013.
695 Intrusion of warm surface water beneath the McMurdo Ice Shelf, Antarctica. *J.*
696 *Geophys. Res. Oceans*, 118, 7036-7048.
- 697 Trowbridge, J. H. ,1992. A simple description of the deepening and structure of a stably
698 stratified flow driven by a surface stress. *J. Geophys. Res. Oceans*, 97, 15529-15543.
- 699 Whitworth, T., and Orsi, A. H., 2006. Antarctic Bottom Water production and export by
700 tides in the Ross Sea. *Geophys. Res. Lett.*, 33, L12609.

701

702 **Appendix A. Model sensitivity to horizontal diffusivity**

703 In numerical models, the background mixing coefficients are chosen based on grid
704 length scale and a time scale for energy dissipation. These parameters should be chosen
705 to preserve the dynamics of interest (Mellor and Blumberg, 1985), damping out
706 fluctuations that are not resolved by the grid (e.g. $2 \Delta x$ waves). In the harmonic case, the
707 background horizontal diffusivity is defined as $(\Delta x/\pi)^2/\Delta t$, where Δt is damping time
708 scale. Our grid resolution is $\Delta x=500$ m, so a practical range for Δt is 3~12 hours,

709 therefore resulting in a horizontal diffusivity coefficient of roughly $0.5\sim 2\text{ m}^2\text{s}^{-1}$. We
710 performed a series of experiments to test the sensitivity of lens thickness near the ice
711 shelf edge to this parameter. Results show that by changing viscosity from 0.5 to $4\text{ m}^2\text{s}^{-1}$,
712 the lens thickness is only shallowed by $\sim 2\text{-}3$ meters, which is an order of magnitude or
713 more less than the amplitude of the simulated signal. In the simulations presented herein,
714 the diffusion coefficient is $0.5\text{ m}^2\text{s}^{-1}$, a value that is smaller than that usually used with the
715 naturally dissipative upstream advection scheme (Shchepetkin and McWilliams, 1998;
716 Dinniman et al., 2003).

717

718 **Appendix B. Details for the basal melting and mechanical forcing by the ice shelf** 719 **edge**

720 Here we briefly summarize the representation of the ice shelf in the model. The
721 ocean water underneath has interactions with the ice shelf through thermodynamics.
722 Under the ice shelf, the upper boundary for the surface model layer is not at sea level
723 because it conforms to the ice shelf base. The hydrostatic pressure gradient force
724 calculation thus accounts for the possibilities that the top layer of the ocean may have a
725 significant slope due to the ice shelf (Shchepetkin and McWilliams, 2003), assuming that
726 the ice is in isostatic equilibrium. While there are concerns about pressure gradient (PG)
727 errors at the ice shelf front in terrain following coordinate models (e.g. Losch, 2008), the
728 PG algorithm used in ROMS (Shchepetkin and McWilliams, 2003) has been explicitly
729 shown to limit these issues in the case of ice shelf fronts (Galton-Fenzi, 2009). A 2-D run
730 without surface forcing or basal melting shows that the PG errors cause only small
731 perturbations to the density field. After several hours of simulation, the solution stabilizes.
732 Changes to the initial density field ($\sim 10^{-4}\text{ kg m}^3$) and the associated velocities ($\sim 10^{-6}\text{ m s}^{-1}$)
733 are essentially small. This suggests that the PG error is not a problem in our simulations.

734 Atmospheric forcing of waters underneath the ice shelf is set to zero, assuming that
735 fluid is isolated from the atmosphere. Friction between the ice shelf and the water is

736 computed as a quadratic stress with a coefficient of 3.0×10^{-3} .

737 At the water-ice shelf interface, a viscous sublayer model is used with three
738 equations representing the conservation of heat, the conservation of salt, and a linearized
739 version of the formula for the freezing point of sea water as a function of salinity and
740 pressure. Free variables in these equations are T_b , S_b , and $\frac{\partial h}{\partial t}$, which stand for
741 temperature, salinity at the ice shelf base, and melting rate, respectively. $\frac{\partial h}{\partial t}$ is <0 for
742 melting and >0 for freezing.

743 The conservation of heat across the ocean-ice shelf boundary is:

$$744 \quad \rho_i(L - C_{pi}\Delta T)\frac{\partial h}{\partial t} = \rho C_{pw}\gamma_T(T_b - T_w) \quad (\text{B.1})$$

745 where ρ_i is ice density (930 kg m^{-3}), L is the latent heat of fusion ($3.34 \times 10^5 \text{ J kg}^{-1}$), C_{pi} is
746 the heat capacity of ice ($2000 \text{ J (kg }^\circ\text{C)}^{-1}$), and ΔT is the temperature difference between
747 the ice shelf interior and the freezing temperature at the ice shelf base. However, in our
748 simulations we did not consider the impact of heat conduction through the ice shelf,
749 therefore $\Delta T=0$ and the ice shelf is assumed to be perfectly insulating. ρ is the density of
750 water, C_{pw} is the heat capacity of sea water at 0°C ($4000 \text{ J (kg }^\circ\text{C)}^{-1}$), γ_T is the turbulent
751 exchange coefficient for heat and is computed as a function of the friction velocity
752 (Holland and Jenkins, 1999), and T_w is the water temperature in the uppermost grid box.

753 The conservation of salt across the ocean-ice shelf boundary is written as:

$$754 \quad \rho_i S_b \frac{\partial h}{\partial t} = \rho \gamma_s (S_b - S_w) \quad (\text{B.2})$$

755 where γ_s is the turbulent exchange coefficient for salt, and is computed as a function of
756 the friction velocity (Holland and Jenkins, 1999), and S_w is the salinity in the uppermost
757 grid box. The linearized equation for the freezing point of sea water (Foldvik and Kvinge,
758 1974) defines T_b as

$$759 \quad T_b = 0.0939 - 0.057 S_b + 7.6410 \times 10^{-4} h \quad (\text{B.3})$$

760 where h is the depth below the sea level.

761 For simplicity, the draft and extent of the ice shelf do not change over time in the

762 model, a reasonable approximation for simulations of this duration also made in previous
763 simulations (Dinniman et al., 2007; Stern et al., 2013).
764

765
766
767
768

3-D experiments	Ice shelf edge	Basal melting	Surface wind forcing
SIS+WIND+BM	Straight	ON	ON
IIS+WIND+BM	Irregular	ON	ON
IIS+BM	Irregular	ON	OFF

769
770
771
772
773
774

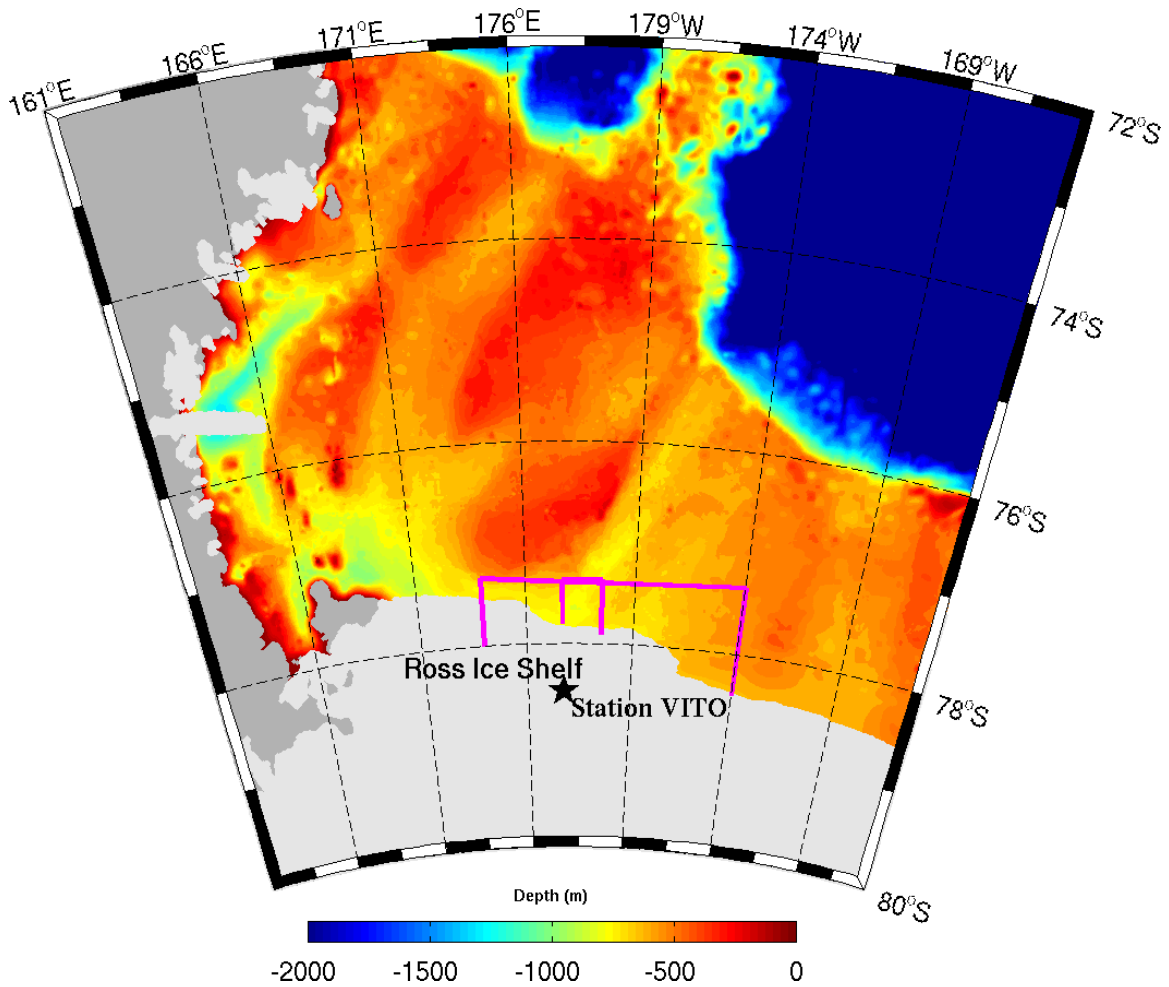
Table 1. List of 3-D experiments performed in this study. In the left column, SIS and IIS stand for “straight ice shelf” and “irregular ice shelf” respectively; BM stands for basal melting.

2-D experiments	Basal melting	Surface wind forcing	Initial condition
WIND	OFF	Observed	CTD 58
BM	ON	OFF	CTD 58
WIND+BM	ON	Observed	CTD 58
HWIND+BM	ON	Observed $\times 1.5$	CTD 58
WIND+BM+WS	ON	Observed	CTD 58, constant density below 50m

775
776
777
778
779

Table 2. List of 2-D experiments performed in this study. In the left column, HWIND, WS, and BM stand for “high wind stress”, “weak stratification”, and “basal melting”, respectively.

780



781

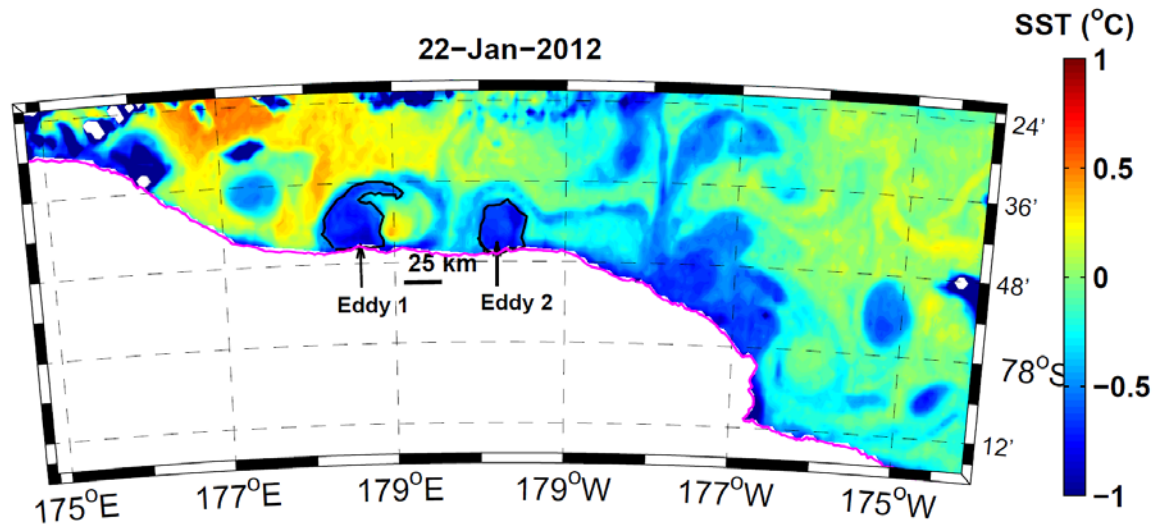
782 Fig. 1. Bathymetric map of the Ross Sea based on Bedmap2 bottom elevation data made
783 available by the British Antarctic Survey (<http://nora.nerc.ac.uk/501469/>). White contours
784 are the 400 m isobath. The Pentagram indicates the location for Antarctic meteorological
785 station VITO. The permanent ice shelf is shown in light gray, and land in dark gray.

786 Domains of the satellite images depicted in Figs. 2 and 3 are shown as solid magenta
787 lines.
788

789
790

791

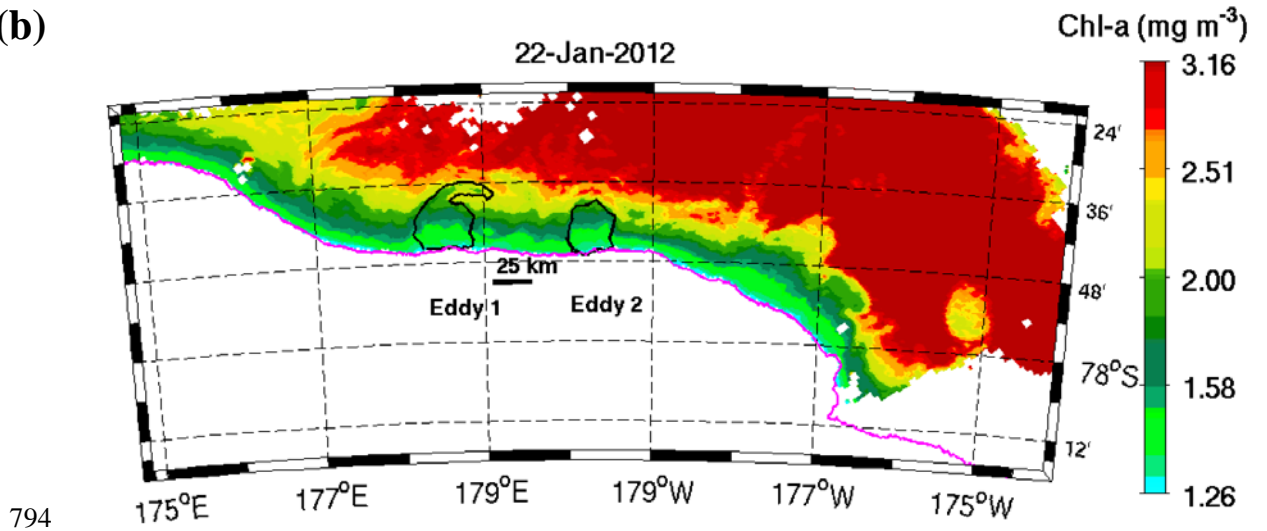
(a)



792

793

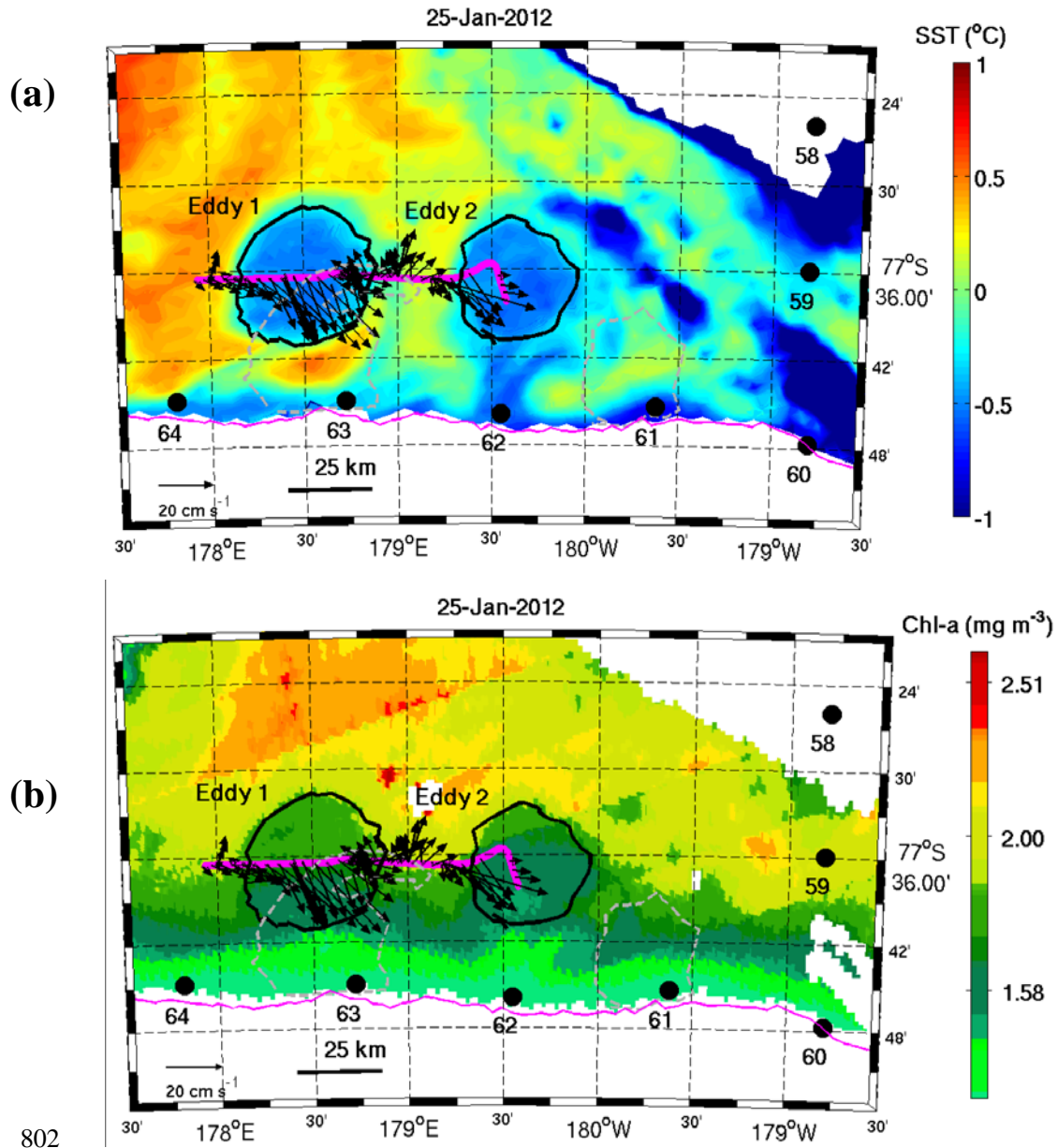
(b)



794

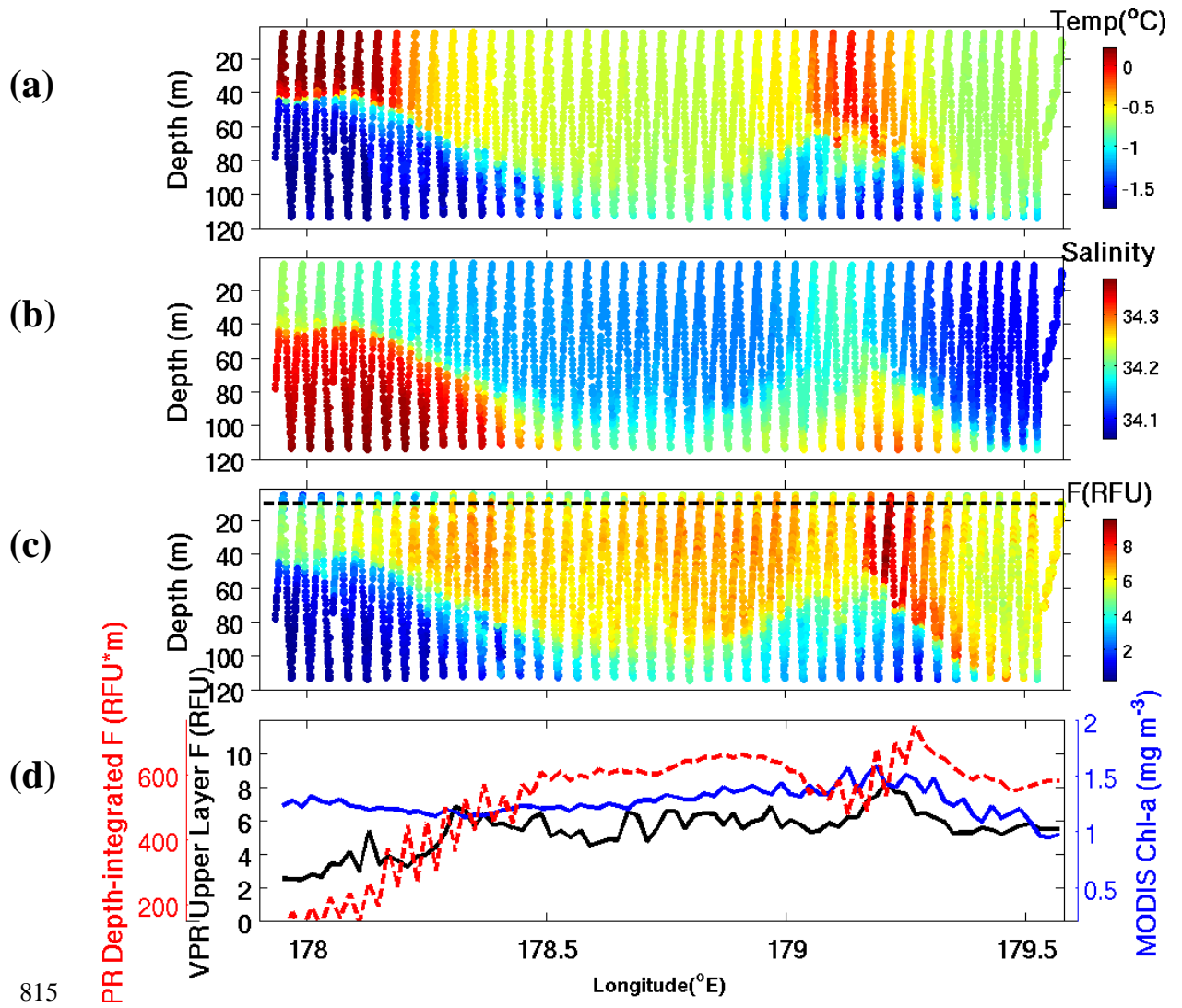
795

796 Fig. 2. Moderate Resolution Imaging Spectroradiometer (MODIS) level 2 (1 km
797 resolution) SST (panel a) and Chl-a (panel b) images for January 22, 2012. Black lines
798 outline the two ice shelf eddies, and magenta lines represent the ice shelf edge estimated
799 from MODIS true color image for January 2012. Satellite data provided by NASA's
800 Goddard Space Flight Center (<http://modis.gsfc.nasa.gov/data/>).



802

803 Fig. 3. Zoom in view of MODIS level 2 SST and Chl-a images for January 25, 2012.
 804 Note that for visualization purposes, the Chl-a concentrations along swaths are projected
 805 into a uniformly spaced longitude-latitude coordinate. The thick magenta lines indicate
 806 the cross-eddy transect on January 26, 2012 depicted in Fig. 4, and thinner magenta lines
 807 represent the ice shelf edge estimated from MODIS true color image for January 2012.
 808 Black solid (gray dashed) lines outline the two ice shelf eddies on January 25 (22), and
 809 black dots indicate CTD station locations (58-64) during the Ross Ice Shelf survey
 810 January 25-26, 2012. Vectors stand for the depth-averaged current over top 150 m during
 811 the survey. Tidal currents in this area are an order of magnitude smaller than the observed
 812 current (Erofeeva et al., 2005) so the ADCP data have not been detided. Velocity scale
 813 factor is shown at the lower left.



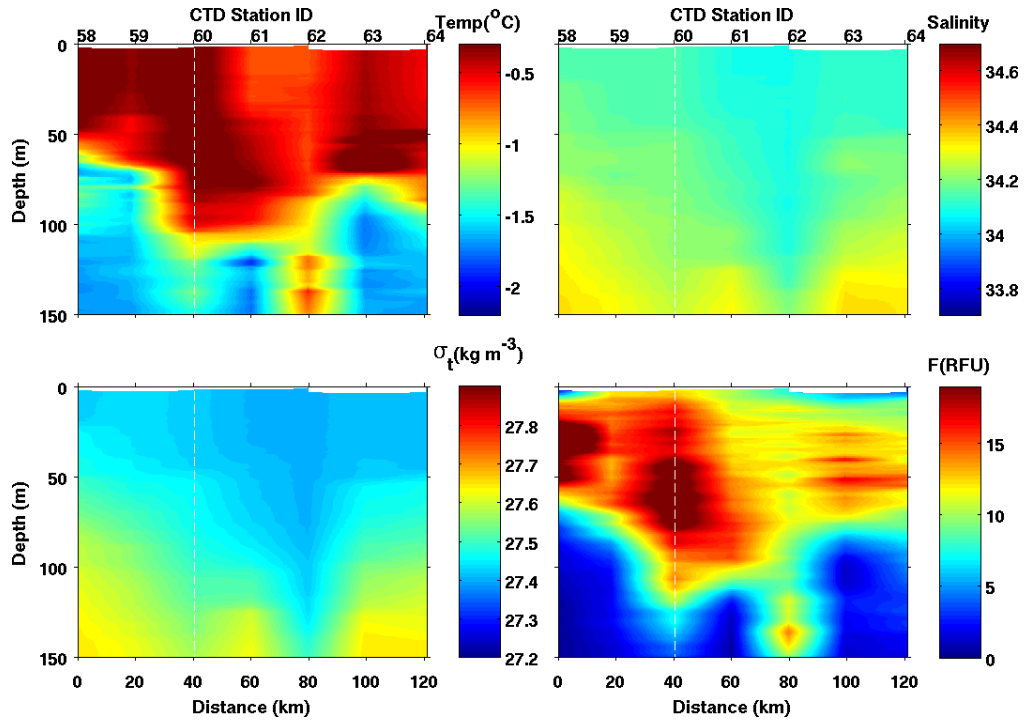
815

816

817 Fig. 4. Profiles of temperature, salinity and fluorescence (F). In panel (c), the depth of the
 818 second optical depth is plotted in black dashed line. F is in relative fluorescence units, or
 819 RFU. Note that this relative scale is not the same as that for the CTD observations
 820 presented in Fig. 5 from the VPR survey depicted by the magenta line in Fig. 3. Bottom
 821 panel shows the weighted VPR fluorescence within the top 10 m (black), MODIS surface
 822 Chl-a concentration extracted along the VPR track (blue), and depth-integrated VPR
 823 fluorescence (red) within the top 100m.

824

825



826

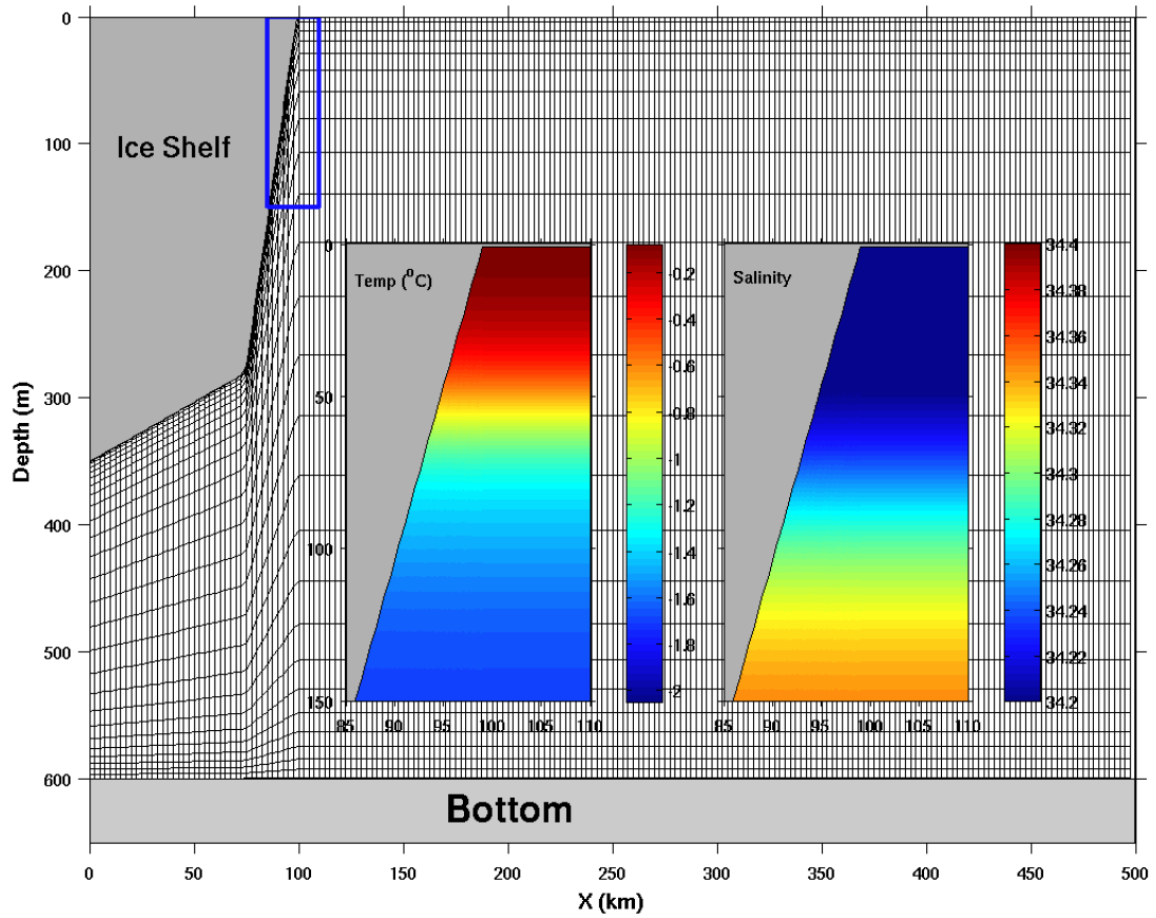
827 Fig. 5. Temperature, salinity, σ_t and fluorescence (F) observations for RIS CTD casts (see
 828 Fig. 3 for station positions). Fluorescence is in relative fluorescence units, or RFU. Note
 829 this relative scale is not the same as that for the VPR observations presented in Fig. 4.

830 The white dashed line indicates the station where the transect orientations shift from
 831 north-south to east-west.

832

833

834



835

836

837

838

839

840

841

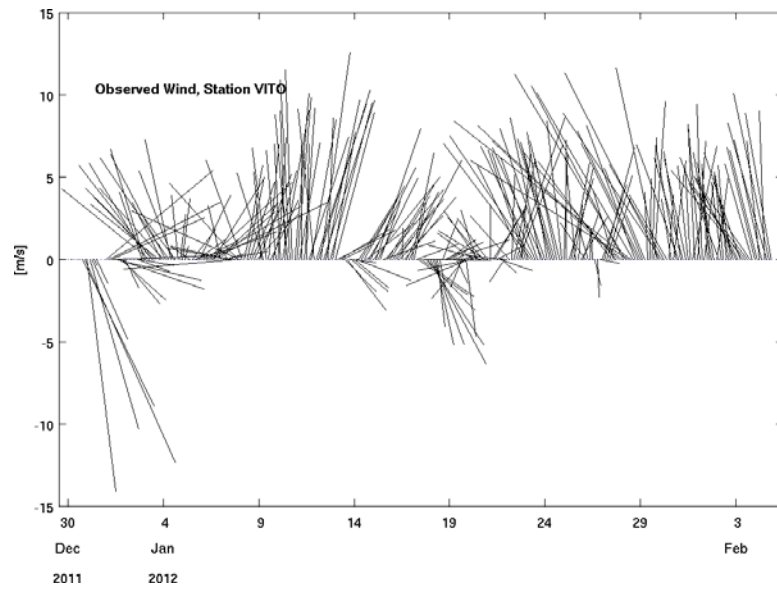
842

843

844

845

Fig. 6. Cross-shelf view of ice shelf configuration and model grid. The grids are decimated such that each cell represents 5 by 4 grid points. Insets show zoomed-in views of the temperature and salinity profiles in the initial condition on the upper part of the ice shelf (blue rectangle).



846
847
848

Fig. 7. 3-hourly 10-meter wind record from meteorological station VITO (see Fig. 1 for station location).

849

850

851

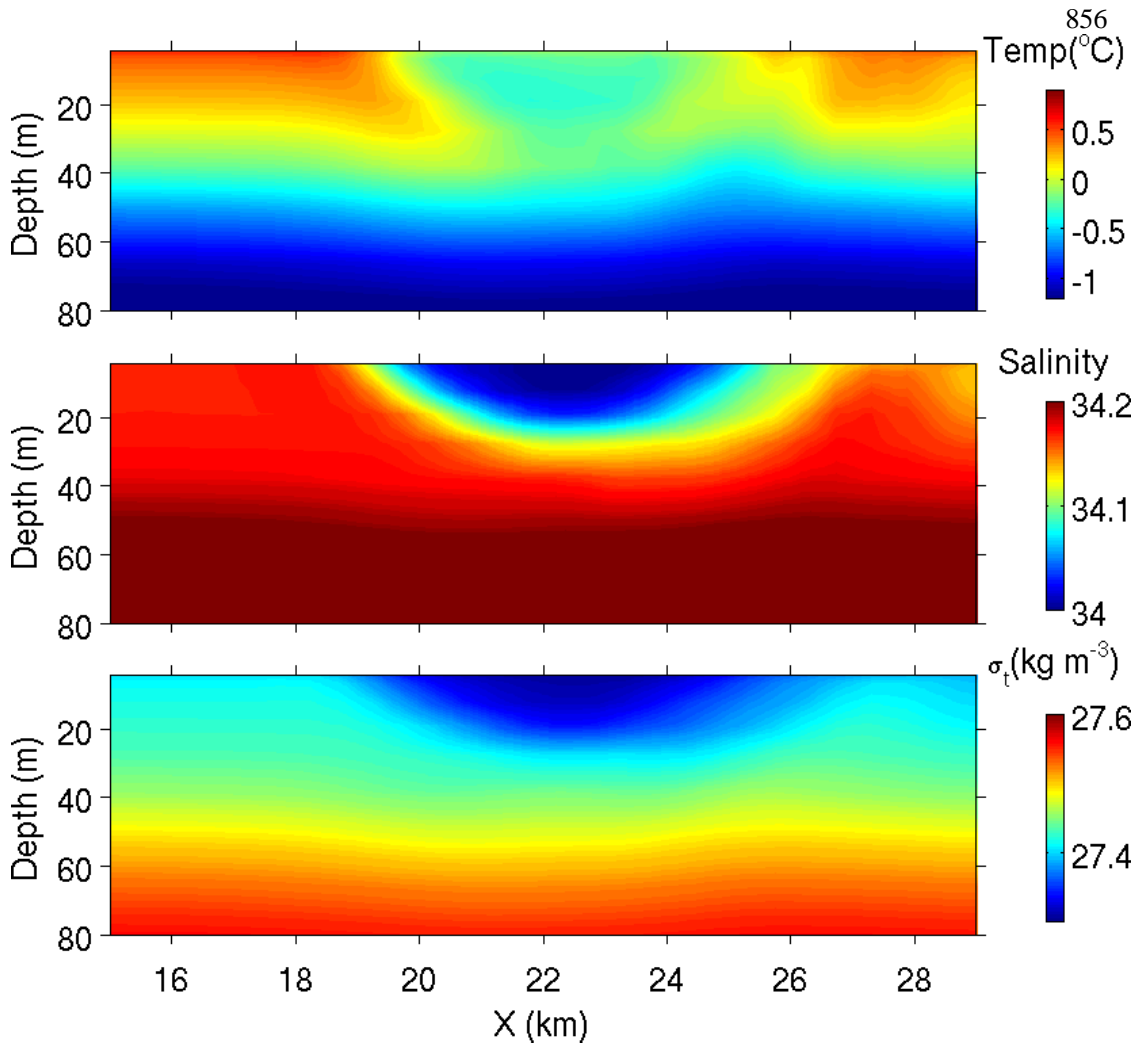
852

853

854

Fig. 8. Snapshots of surface temperature and salinity (surface velocity vectors overlaid) at model day 25 listed in Table 1: (a, b) SIS+BM+WIND; (c, d) IIS+BM+WIND; (e, f) IIS+BM. The magenta line in panels c and d indicates the location of a cross-eddy transect shown in Fig. 9.

855

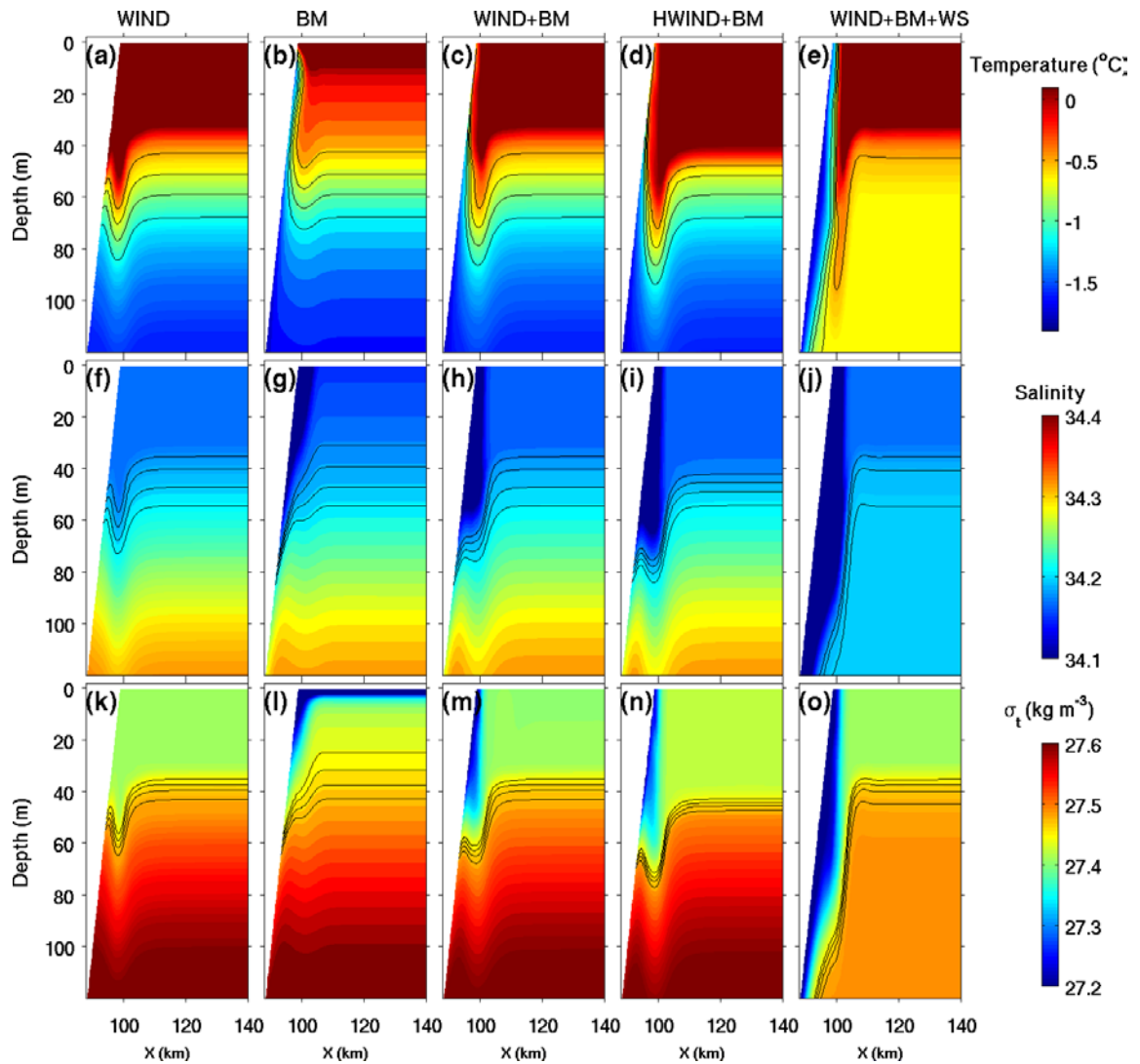


881

882

Fig. 9. Vertical transect of temperature, salinity and σ_t for the cross-eddy transect indicated in Fig. 8.

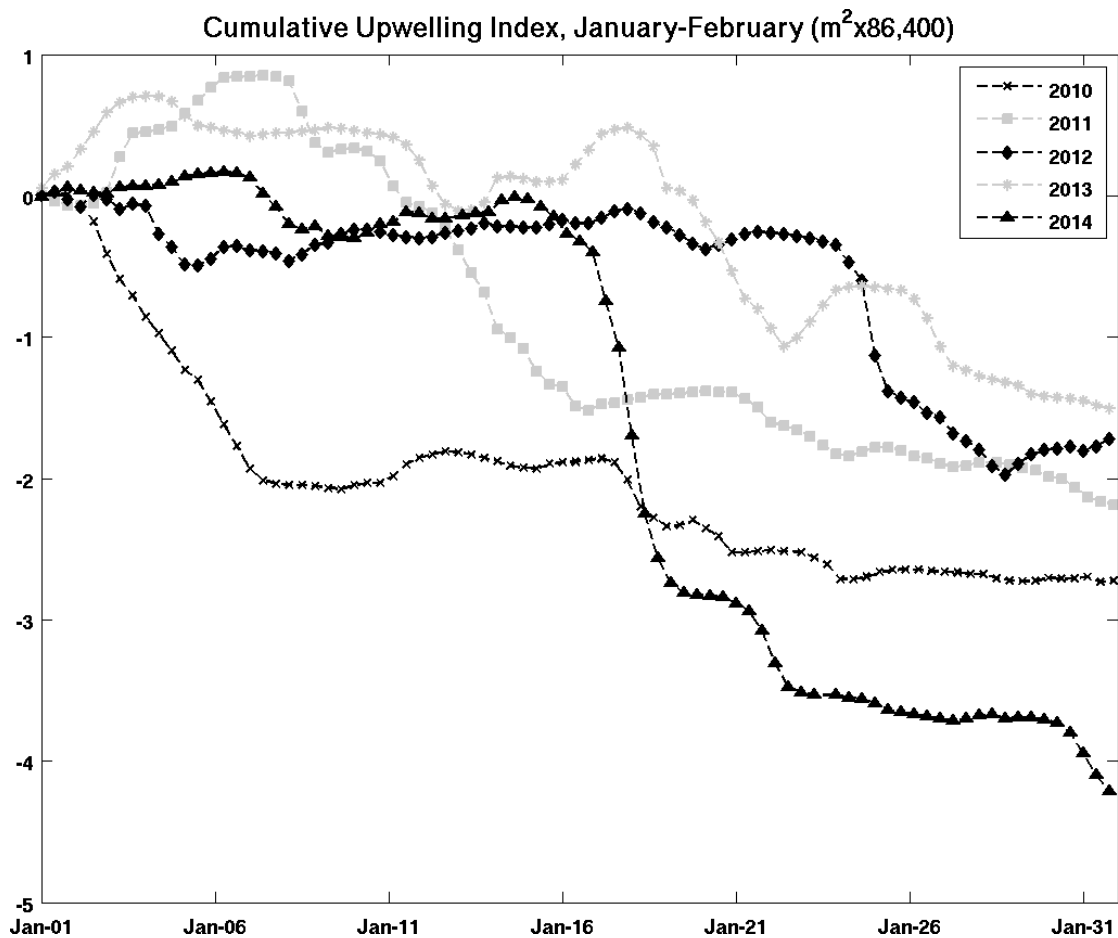
883



884
 885
 886
 887
 888
 889
 890
 891
 892
 893
 894
 895

Fig. 10. Snapshots of temperature, salinity and σ_t on model day 29.5 for 2-D experiments listed in Table 2: (a, f, k) WIND; (b, g, l) BM; (c, h, m) WIND+BM; (d, i, n) 2D HWIND+BM; (e, j, o) 2D WIND+BM+WS. Solid contours highlight key isotherms (-1.1 to -0.5 °C at intervals of 0.2 °C), isohalines (34.18 to 34.21 at intervals of 0.01), and isopycnals (27.45 to 27.48 kg m^{-3} at intervals of 0.01 kg m^{-3}).

896
897
898
899



900
901
902
903
904

Fig. 11. Cumulative Upwelling Index (CUI) for the Januaries in 2010-2014.